20th AIAA/CEAS Aeroacoustics Conference (35th AIAA Aeroacoustics Conference), 16-20 June 2014, Atlanta, Georgia

An Experimental Investigation of the 30P30N Multi-Element High-Lift Airfoil

Kyle A. Pascioni* and Louis N. Cattafesta†
Florida Center for Advanced Aero-Propulsion (FCAAP)
Florida State University, Tallahassee, FL, 32310

Meelan M. Choudhari‡
NASA Langley Research Center, Hampton, VA, 23681

High-lift devices often generate an unsteady flow field producing both broadband and tonal noise which radiates from the aircraft. In particular, the leading edge slat is often a dominant contributor to the noise signature. An experimental study of a simplified unswept high-lift configuration, the 30P30N, has been conducted to understand and identify the various flow-induced noise sources around the slat. Closed-wall wind tunnel tests are performed in the Florida State Aeroacoustic Tunnel (FSAT) to characterize the slat cove flow field using a combination of surface and off-body measurements. Mean surface pressures compare well with numerical predictions for the free-air configuration. Consistent with previous measurements and computations for 2D high-lift configurations, the frequency spectra of unsteady surface pressures on the slat surface display several narrow-band peaks that decrease in strength as the angle of attack is increased. At positive angles of attack, there are four prominent peaks. The three higher frequency peaks correspond, approximately, to a harmonic sequence related to a feedback resonance involving unstable disturbances in the slat cove shear layer. The Strouhal numbers associated with these three peaks are nearly insensitive to the range of flow speeds (41-58 m/s) and the angles of attack tested (3-8.5°). The first narrow-band peak has an order of magnitude lower frequency than the remaining peaks and displays noticeable sensitivity to the angle of attack. Stereoscopic particle image velocimetry (SPIV) measurements provide supplementary information about the shear layer characteristics and turbulence statistics that may be used for validating numerical simulations.

Nomenclature

b	Airfoil span [m]	TKE	Turbulent kinetic energy
c	Airfoil stowed chord [m]	U_∞	Freestream velocity [m/s]
C_p	Coefficient of pressure	$\|V\|$	Velocity vector magnitude [m/s]
f	Frequency [Hz]	u, v, w	Velocity components [m/s]
G	Autospectral density function [Pa^2/Hz]	x	Chordwise distance [m]
L_γ	Coherence length [m]	Δz	Spanwise distance [m]
m, n	Transducer indicies	α	Geometric angle of attack [°]
N	Total number of transducers	γ^2	Ordinary coherence function
PSD	Power spectral density [Pa^2/Hz]	ω_z	Spanwise vorticity [1/s]
q	Dynamic freestream pressure [Pa]	$\langle\cdot\rangle$	Ensemble average of quantity
Re_c	Reynolds number based on c	**Superscript:**	
s	Slat chord [m]	$()^*$	Nondimensional units
St_s	Strouhal number based on s	$()'$	Fluctuating quantity

*Graduate Research Assistant, Dept. of Mechanical Engineering, Member, AIAA
†Eminent Scholar Endowed Professor, Dept. of Mechanical Engineering, Associate Fellow, AIAA
‡Aerospace Technologist, Computational Aerosciences Branch, Mail Stop 128, Associate Fellow, AIAA.

I. Introduction

High-lift devices have become an important contributor to aircraft noise due to the increase in engine bypass and other low noise propulsive technologies. In several civil transport configurations, the leading edge slat can dominate the airframe component of the radiated acoustic field during approach.[1] Furthermore, new vehicle concepts, such as the Hybrid Wing Body (HWB), are projected to omit the use of the trailing edge flap and increase the size of the leading edge slats,[2] thus likely increasing its noise signature.

An experimental investigation is performed on a high-lift system, the 30P30N,[3,4] which is a simplified unswept configuration composed of three elements. As is the case for the majority of high-lift systems, the leading edge slat and trailing edge flap are deployed to improve lift. The slat extends the lift curve (i.e., lift coefficient versus α) to a larger stall angle, while the flap increases lift at a given α shifting the curve up. Although this configuration provides the necessary aerodynamic characteristics, flow unsteadiness is prominent near the slat, lending to a more intense acoustic field. This field is broadband in nature with several narrow-band peaks around $St_s \approx 1$ to 3. Specific noise sources have been hypothesized, but their origin and relative magnitude is unclear. For example, the shear layer emanating from the lower cusp convects and rolls up into discrete spanwise vortices. These coherent structures impinge on the lower slat surface creating a recirculation region between the fluid passing through the slat and main element gap. The surface impingement of these vortical structures coupled with a cavity-like resonance of the slat cove[5–7] is a prime noise source candidate (See Fig. 1 of Choudhari et al.[8]). Also, the geometric gap between the slat and main element is possibly the source of a lower frequency "breathing" effect, and could be due to an oscillating reattachment position. The slat trailing edge is another feature expected to generate a high frequency tone due to vortex shedding from its small (but finite) thickness.[9] In certain circumstances, amplification of this tone is possible[10] and can become the largest amplitude spectral feature. Scattering off the downstream element is also likely to influence the farfield acoustics.

Physics-based prediction of slat noise is still in a relatively early stage, although promising progress has been made in recent years. Guo[2] developed an analytical model by using the acoustic analogy, which provides good agreement with experimental trends. Joint computational and experimental studies such as those described in references 8, 11, 12, and 13 will allow further improvement and validation of such physics based models. In particular, additional measurements of the slat cove aerodynamics and the radiated acoustic field are deemed necessary to enable a definitive validation of physics-based tools for the prediction of slat noise.

A number of techniques to reduce the impact of slat noise have been investigated in the past. A partial list includes a slat-cove filler, which may be either partial[14] or completely sealed[1,15,16] and porous surface treatments[17,18] that seek to attenuate scattering and cove resonance. Such devices show promise, but a fuller understanding of the underlying physics will help direct the design choices toward optimal performance.

This work focuses on characterizing the leading edge slat region of the 30P30N geometry. An overview of the facility, scaled model, and experimental methods is first discussed. The mean and fluctuating pressure data is then analyzed to demonstrate Reynolds number and angle of attack dependencies. Finally, stereoscopic PIV of the slat cove is presented for off-body flow characteristics and followed by conclusions.

II. Experimental Setup and Methods

This section begins with a description of the Florida State Aeroacoustic Tunnel (FSAT) as well as the aerodynamic model used. Then, specifics on measurements techniques, instrumentation, and acquisition parameters will follow.

II.A. Florida State Aeroacoustic Tunnel

The Florida State Aeroacoustic Tunnel (FSAT) is an open-circuit anechoic wind tunnel as shown in Figure 1. A 450 hp centrifugal blower provides test section flow speeds from 15 m/s to 75 m/s. The test section with dimensions of 0.914 m×1.219 m×3.048 m (Height×Width×Length) is housed inside an ISO-3745 certified 250 Hz anechoic chamber. Five flow conditioning screens decreasing in mesh size minimize turbulence while a honeycomb section straightens the incoming jet. Flow non-uniformity and turbulence intensity is measured to be $< 1\%$ and $< 0.1\%$, respectively, for all flow speeds. An open-jet configuration allows for acoustic measurements within the anechoic chamber, i.e., outside of the nozzle jet. Because the acoustics were not the focus of the present experiments, the optional closed-wall test section was leveraged to avoid the substantial

modification of model aerodynamics due to deflection of the nozzle jet in an open-jet configuration. As shown later, the closed-wall test section enables measurements at moderate angles of attack (reflecting the high-lift settings relevant to an aircraft's approach for landing) while matching the aerodynamic loading in an infinite free stream (i.e., open-air or flight configuration).

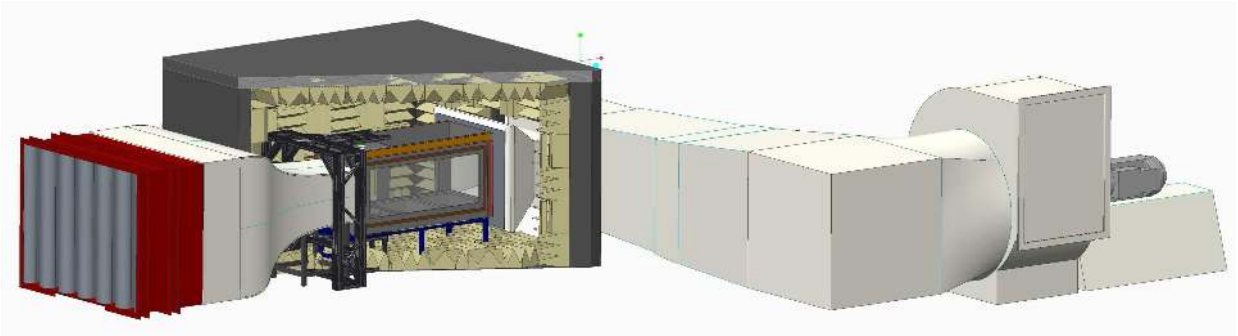

Figure 1. Florida State Aeroacoustic Tunnel (FSAT). Note: Flow direction is left to right, and the anechoic chamber is cut for illustration.

II.B. High-Lift Model

The 30P30N is a well studied high-lift geometry numerically;[8,11,13,19] however, a thorough experimental database is lacking at this stage (see Refs. 12 and 19 for summaries of previous measurements of this model). Shown in Figure 2, the airfoil used in the present experiments corresponds to a two dimensional model with a stowed chord $c = 0.457$ m. The slat chord equals $s = 0.15c$ whereas the flap chord is $0.3c$ and both elements are deflected 30° relative to the main element chord. The stowed chord is based on the cruise configuration, i.e., when both the slat and the flap are in retracted positions. The model is mounted vertically in FSAT, spanning the full height of the test section, and is centered in the normal direction. The leading edge of the model is located 0.3 m downstream of the nozzle exit. Other geometric settings such as the gap and overhang of the slat and the flap are fixed at identical values as those in Jenkins et al.[12] and are summarized in Table 1. The angle of attack is referenced to the main element chord. At the maximum angle of attack used in the present tests ($\alpha = 8.5°$), the blockage ratio (defined as the fraction of tunnel cross-section blocked by the model) is 12.5%. Even though boundary layer trips are known to influence the aeroacoustic characteristics of 2D high-lift models unless the Reynolds number is sufficiently large, the initial measurements reported in this paper were obtained without any trips on any of the three elements comprising the 30P30N configuration.

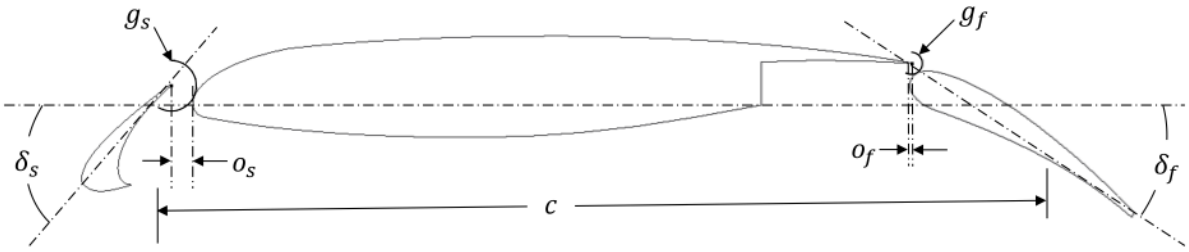

Figure 2. Definition of geometric parameters.

II.C. Instrumentation and Data Acquisition

Instrumentation and acquisition parameters of the three measurement techniques are provided in this section. Experimental issues encountered and how they are resolved are also discussed.

II.C.1. Steady Pressure

A total of 122 static pressure ports populate the airfoil surface including all three elements. As seen in Figure 3, the majority of these ports are located along the mid-span plane. However, two spanwise arrays

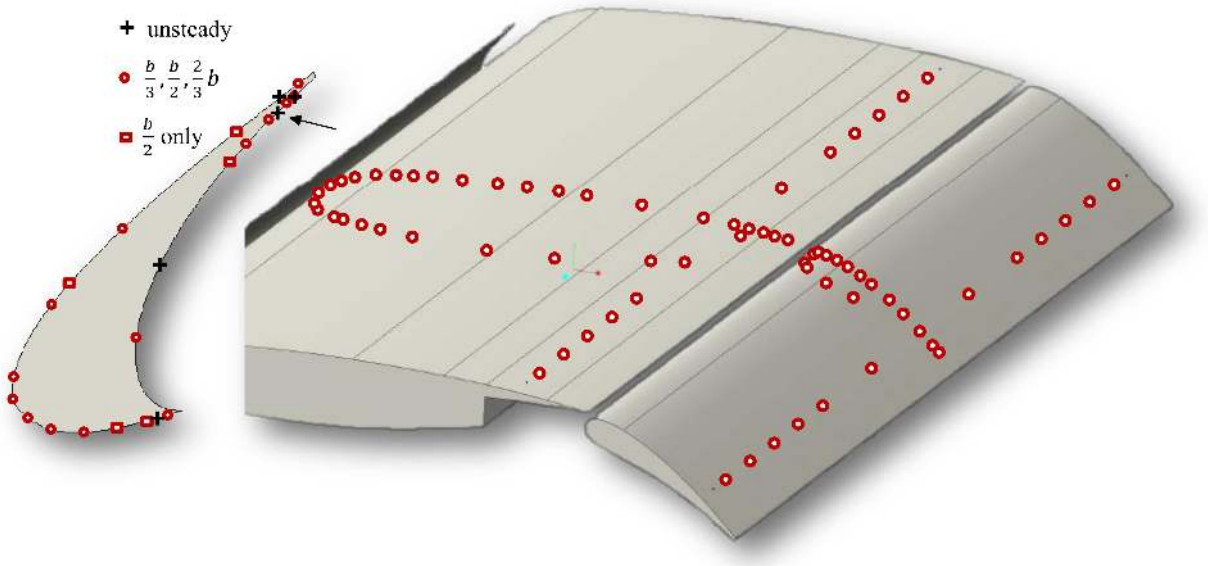

Figure 3. Steady and unsteady pressure measurement locations. Legend corresponds to slat only, and arrow on slat profile denotes the unsteady spanwise array.

Table 1. Geometric parameters (gap and overhang values are specified as percentage of stowed chord, c).

Stowed chord	c	0.457 m
Slat deflection angle	δ_s	30°
Flap deflection angle	δ_f	30°
Slat gap	g_f	2.95%
Flap gap	g_f	1.27%
Slat overhang	o_s	−2.5%
Flap overhang	o_f	0.25%

of static pressure ports are also located near the aft region of the main element and the flap at $x/c = 0.75$ and $x/c = 1.072$, respectively. Two additional chordwise arrays are installed on the slat at $z/b = 1/3$ and $z/b = 2/3$, respectively. The ports are flush to the surface and have a diameter of 0.5 mm each. Tubing is connected to two 16-channel Scanivalve pressure scanners (Type DSA3217, ±1psi differential) with an uncertainty of ±8 Pa. At 2 Hz, 100 samples are acquired throughout multiple tunnel runs, which are necessary as the ports outnumber the available channels. The reference pressure of the scanners is adjusted using a known source in order to enable the peak suction pressure over the main element to stay within the measurable range.

The presence of the model is found to influence the freestream measurements of the Pitot-static probe. Therefore, only the total pressure is measured using the probe. To obtain the static freestream pressure, four static ports are drilled upstream (centered on each of the tunnel walls) and flush mounted to the inlet contraction surface. These ports are connected to one another via tubing to provide a single output, which is the average static pressure from these four locations. However, since the tunnel cross section is larger here, an area correction of 1.256:1 derived from the incompressible continuity equation is applied. Boundary layer growth, which can virtually change the cross sectional area, is assumed to be small between the static ports and the model.

II.C.2. Unsteady Pressure

Several unsteady pressure transducers, Kulite® Type LQ-062-2PSID, are installed flush to the slat surface to quantify the local fluctuations. All signals are differential with custom in-line amplifiers. Each sensor is statically calibrated throughout its pressure range to determine their respective sensitivity. Nominal values are around 0.3 mV/Pa and are within 3% of the original calibration.

Transducers are dispersed around the slat at five different chord positions. A spanwise array denoted by the arrow in Figure 3 is located just upstream of the trailing edge along the slat pressure surface, i.e., in the vicinity of the shear layer reattachment locations within the relevant range of angles of attack ($-2.5° < \alpha < 8.5°$). The spanwise array consists of six closely spaced sensors within a spanwise segment of 11.9 mm near the mid-span location, along with an additional eight sensors placed at intervals of 25 mm, nominally.

Signal acquisition employed a NI PXI-1031 chassis that housed two NI PXI-4498 cards. Each card allows simultaneous sampling with 24-bit resolution along with embedded antialiasing filters. Signals are acquired for 60 s at 65,536 samples/s. For spectral considerations, the time record was split into blocks of 4,096 samples resolving a 16 Hz binwidth. A Hanning window with 75% overlap resulted in 2.24% uncertainty in the random component of the autospectra. Power spectral density results presented in the next section are normalized by their respective freestream conditions by

$$St_s = \frac{fs}{U_\infty}, \tag{1}$$

$$PSD^* = PSD\frac{1}{q^2}\frac{U_\infty}{s}. \tag{2}$$

II.C.3. SPIV

Stereoscopic Particle Image Velocimetry (SPIV) provides information about the slat cove recirculation and shear layer. The system uses two 5-MP sCMOS cameras along with a 200 mJ dual pulse Nd:Yag laser (Quantel Evergreen HP). The cameras have 16-bit resolution and are equipped with 105 mm lens. The laser sheet with a thickness of approximately 2 mm is produced using a cylindrical lens and a spherical lens that are aligned in series. LaVision DaVis software provides timing and initial image processing. Geometric constraints on viewing access forces the lines of sight of the two cameras to be 45° and 70°, respectively, from the laser sheet plane. Also, the cameras are in backscatter mode resulting in lower particle image intensity due to the directivity of particle light scattering. Conversely, large reflection bands incident on the model surface inhibit particle correlations close to the surface. Since the camera positions are fixed, reflections are minimized via orange fluorescent tape in the slat cove (0.1 mm thick) in conjunction with 532 nm bandpass filters on the cameras.

The seed is introduced just downstream of the flow conditioning screens. Olive oil is atomized using a Laskin nozzle producing $\approx 1\mu$m diameter particles. The particles tend to get trapped in the cove recirculation

but not in the remaining field of view. To obtain enough vectors for the averaging process, 2,000 image pairs are acquired at 15 Hz. Turbulence statistics are found to be converged provided at least 800 averages per window are available. The field of view is 105×122 mm and processed using a final window size of 24×24 pixels. The window size is chosen upon inspection by minimizing its size while ensuring (in an averaged sense) 5–10 particles are present per window. 50% overlap is imposed resulting in a vector resolution of 0.45 mm.

During the image processing stage, several issues were found. First of all, the geometry of the slat cove causes the laser reflections to converge in the region of interest. Prior to the correlation process, an image subtraction is usually performed to minimize background and/or intensity non-uniformity effects. The minimum intensity of each pixel across all images is found and subtracted from each individual image, pixel by pixel. The result was useful, however, a second attempt is made by using the average intensity (ensembled in all images) of each pixel and proved more effective. Therefore, the second subtraction scheme was imposed. Secondly, due to the nature of an open-circuit tunnel, seeding was often sporadic and its concentration varied significantly in the free stream. To combat the outliers, the images were post-processed by a Multivariate Outlier Detection (MVOD)[20] algorithm, which effectively deletes the majority of non-physical vectors.

III. Results

Data acquired using a combination of steady pressure ports, unsteady pressure transducers, and stereoscopic particle image velocimetry are processed and presented. Key features and relationships are discussed to provide insight into the slat cove flow field.

III.A. Mean Surface Pressure

Mean surface pressure is acquired along the model chord at center span. Figure 4 shows the coefficient of pressure for three angles of attack at a Reynolds number based on the stowed chord, $Re_c = 1.71 \times 10^6$. As angle of attack is increased, the stagnation point on the slat moves away from the slat trailing edge, i.e., toward the cusp. This causes the flow to be accelerated around the curved leading edge, increasing aerodynamic loading. Similarly, the stagnation point on the main element moves toward the pressure side. Reasonable agreement is found with computations performed by Choudhari et al.[21] who modeled an "infinite" freestream domain, i.e., the open-air configuration. The most noticeable discrepancy between the measured and computed pressure distributions is observed on the main wing at $x/c \approx 0.25$ and may be due to differences in the size of the leading edge separation bubble near $x/c = 0.15$. However, pressure recovery on the main element agrees well. The flap surface pressure is nearly independent of the angle of attack as it is primarily a function of its deflection angle, which is held fixed at 30°.

Although the center span ports did not show signs of tunnel interference, wall effects can be significant for low aspect-ratio high-lift models.[22] Due to the strong adverse pressure gradients on the model surface, especially the flap, the wall boundary layer tends to separate causing a junction vortex. The result is quantified using the spanwise static ports in Figure 4d showing slight divergence from a purely two dimensional flow. Oil flow visualization also confirmed the separation is similar to that seen by Rumsey et al.[22] Since the fluid near the walls is decelerated, conservation of mass forces the flap suction peak to increase slightly. As the junction vortices become larger with flow speed, the pressure coefficient corresponding to the flap suction peak increased by 0.12 from $Re_c = 1.2 \times 10^6$ to 1.71×10^6. To combat this, wall suction is often used[3,22] to ensure a more uniform flow. However, the present results without suction prove useful since the centerline pressure distribution is not significantly affected and integrated quantities (i.e., lift and drag) are not a prime concern. The surface pressure distribution over the slat is used to evaluate the two dimensionality of the mean flow. Chordwise arrays of pressure taps at $b/3$ and $2b/3$ span are compared with the centerline distribution in Figure 5 and the differences in pressure coefficient are found to be less than 0.1. The spanwise homogeneity of the flow over the middle one third of the model span will be used in future decisions related to the area of integration when microphone phased array measurements are used to estimate the acoustic spectra associated with slat cove noise.

III.B. Unsteady Surface Pressure

Unsteady pressure signals are acquired at five different chordwise locations and summarized in Figure 6. The broadband levels vary by an order of magnitude when comparing locations inside and outside of the

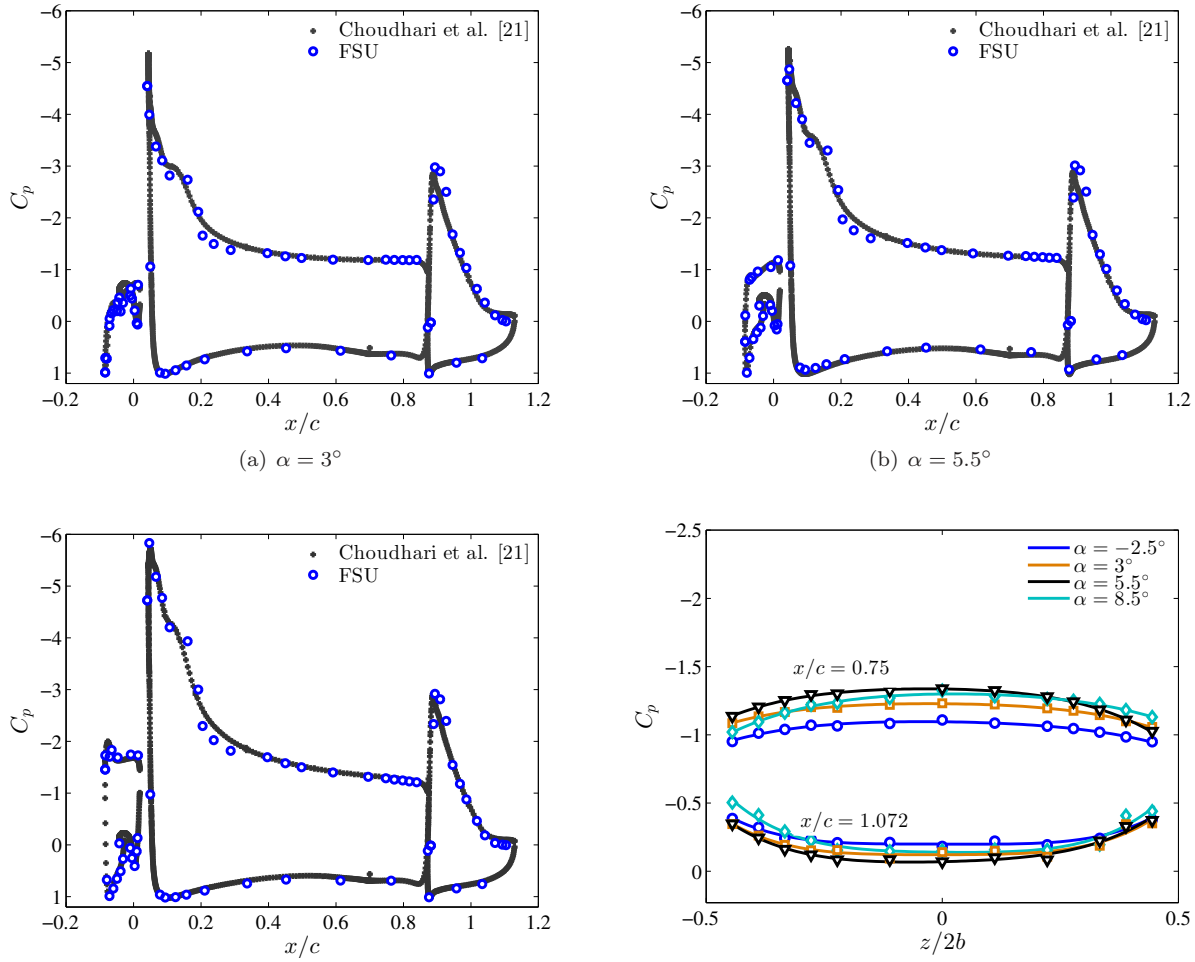

(a) $\alpha = 3°$ (b) $\alpha = 5.5°$

(c) $\alpha = 8.5°$ (d) Experimental spanwise pressure distribution

Figure 4. Centerline surface pressure compared to Choudhari et al.[21] (a-c) and (d) spanwise arrays on the main element and flap.

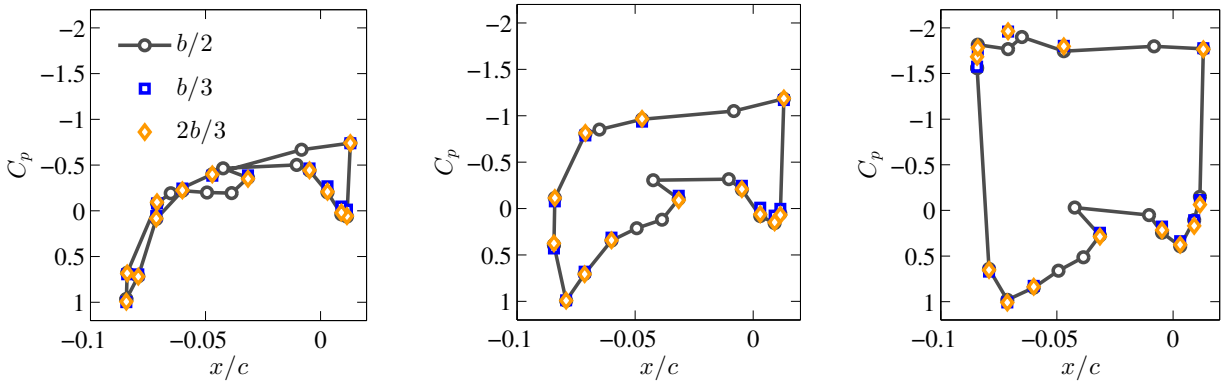

(a) $\alpha = 3°$ (b) $\alpha = 5.5°$ (c) $\alpha = 8.5°$

Figure 5. Slat surface pressure illustrating spanwise uniformity.

slat cove. The largest overall levels are near the shear layer reattachment point suggesting the cove region is the source of the most prominent fluctuations. The suction side exhibits the lowest levels of pressure fluctuations as they are not directly exposed to the high amplitude vorticity structures in the slat shear layer. Narrow-band peaks are present in the frequency spectra at all locations and are likely to be caused by resonant oscillations due to flow acoustic interactions within the cove. Specifically, the feedback loop associated with such interactions can give rise to global instabilities that are known as Rossiter modes[23] in the context of open cavity flows. The dynamics of the slat cove flow is qualitatively similar to that of a grazing flow past an open cavity. Analogous to the cavity flow configuration, the shear layer bounding the cove region impinges on the slat underside, causing acoustic waves to propagate back toward the cusp, which, in turn, excite new hydrodynamic structures within the shear layer, closing the feedback loop.

Figure 7 shows how the amplitudes of the narrow-band peaks near the reattachment location are reduced with an increasing angle of attack. One could argue the reattachment point is displaced away from the measurement location (due to the fact that the transducer positions are fixed) as the size of the recirculation region changes. The numerical simulations by Choudhari et al.[21] show a global reduction of rms C_p on the slat with increasing α. Furthermore, the peak amplitudes are also reduced at the transducer locations outside of the cove (locations 1 and 5). The Strouhal numbers of the dominant peaks are summarized in Table 2. Note the $St_{s,1}$ peak increases in frequency with α, while $St_{s,2-4}$ decrease in frequency. This relationship is also seen by Chen and Fang[24] on a flat plate, and suggests there is a more appropriate length scale, one that is at least a function of α. Possible scales include the frontal slat length normal to the freestram ($s\sin(\delta_s - \alpha)$) or the path length of the shear layer. It also suggests the flow feature responsible for $St_{s,1}$ is likely distinct and independent of $St_{s,2-4}$ mechanism(s).

The effect of tunnel speed on the frequency spectrum at location 3 (which is in the vicinity of the reattachment point) is shown in Figure 8 for $U_\infty = 41$ to 58 m/s ($Re_c = 1.2 - 1.71 \times 10^6$). Figure 8a shows the spectrum in term of dimensional quantities, whereas the nondimensional representation of the same data (based on Equations 1 and 2) is shown in Fig. 8b. The effect of flow speed is manifested via both the Reynolds number and the Mach number. Although the Reynolds number is expected to be the primary influence on the unsteady flow characteristics, the Mach number would also play a role when flow-acoustic interaction is present such as that expected in the case of the narrow-band peaks. The approximate collapse of the various curves in Fig. 8b indicates that the broadband portion of the spectrum at location 3, at least, scales with the freestream quantities used in Equations 1 and 2. An approximate Strouhal scaling as indicated in these equations also applies to the narrow-band peaks. Specifically, the Strouhal number for the peaks changes very slightly with the flow speed and the level of these peaks changes a bit more significantly when the flow speed is varied. For example, the maximum of the main spectral peak at the lowest angle of attack of interest ($\alpha = 3^\circ$) is observed at an intermediate range of Reynolds numbers. The weak variation in the Strouhal number values of the narrow-band peaks is consistent with the fact that the Mach number remains small at all flow speeds.

The intensity of noise radiation is sensitive to the spatial coherence scale of the source fluctuations at any given frequency. Therefore, the spanwise coherence characteristics of the slat pressure fluctuations must be investigated in addition to their frequency spectra at individual locations. Such information also provides useful guidance in determining an appropriate spanwise extent for the computational domain. The coherence between transducer locations m and n is defined as

$$\gamma^2_{m,n} = \frac{G_{m,n}}{|G_{m,m}||G_{n,n}|} \text{ for } m = 1 \text{ and } n = 1, 2, 3, ..., N, \tag{3}$$

where N is the number of spanwise transducers in question. The coherence between selected transducer pairs is plotted in Figures 9-11 as a function of the Strouhal number and angle of attack. In each plot, the spanwise location of the reference transducer is held fixed ($m = 1$). Furthermore, the coherence function at smaller spanwise separations is shown in part (a) of each figure, whereas part (b) shows the coherence at larger spanwise separations. The coherence decreases with spanwise separation in all cases. More interestingly, a larger coherence is observed at the lower angles of attack, regardless of whether the frequency parameter corresponds to the broadband portion of auto-spectra or to the narrow-band peaks. The spanwise variation of the coherence function at a fixed frequency and angle of attack can be reasonably (albeit imperfectly) approximated by a Gaussian curve as found during the numerical simulations of Lockard and Choudhari:[13]

$$\gamma^2(St_s) = \exp\left(-\left(\frac{\Delta z}{L_\gamma(St_s)}\right)^2\right). \tag{4}$$

The above approximation allows one to define the coherence length, L_γ, as a single measure of the spanwise coherence at any given frequency.

In the general sense, this function can be fit using the values calculated by Equation 3. The assumption of homogeneity of the fluctuations across the spanwise array allows a larger dataset to be used, which effectively changes the indices of the coherence calculation to $m, n = 1, 2, 3, ..., N$. Although additional scatter is evident, this method is found to be more robust to sensor noise and effects of spectral resolution. Figure 12a is an example of the functional fit for all coherence pairs at two Strouhal numbers for $\alpha = 3°$. Gathering the computed coherence lengths collapses the data as shown in Figure 12b. The peaks seen here are identical in Strouhal number to the spectral plots, which implies that the spectral peaks have very large coherence lengths, comparable to the slat chord. The fitting function may lead to significant errors in determining the numerical values of the spanwise coherence, but the frequency dependence of the coherence length clearly highlights which frequency bands correspond to spectral peaks. The possibility of using an improved curve fit will be investigated in future studies.

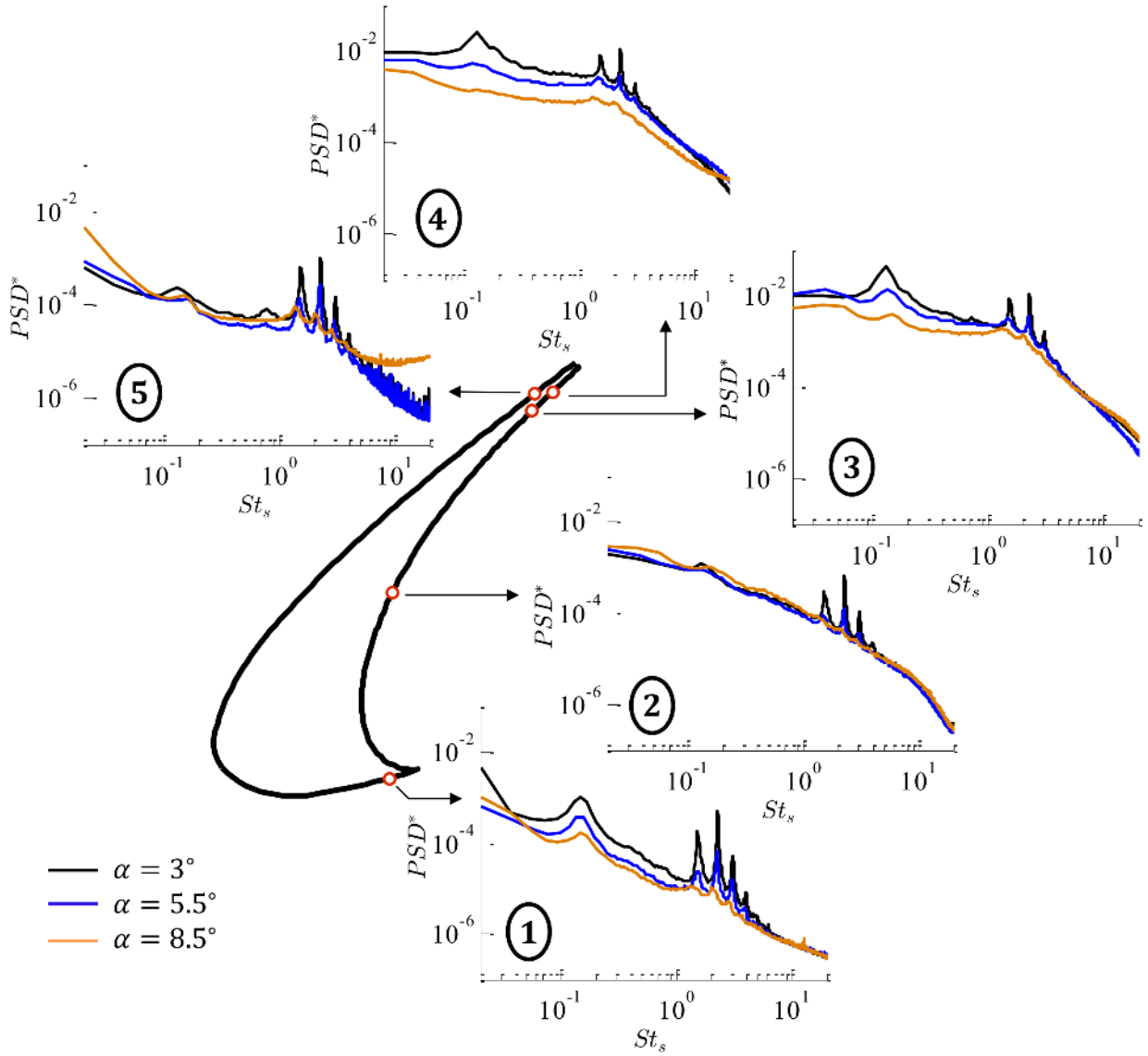

Figure 6. Spectra of pressure fluctuations at various locations for $Re_c = 1.71 \times 10^6$.

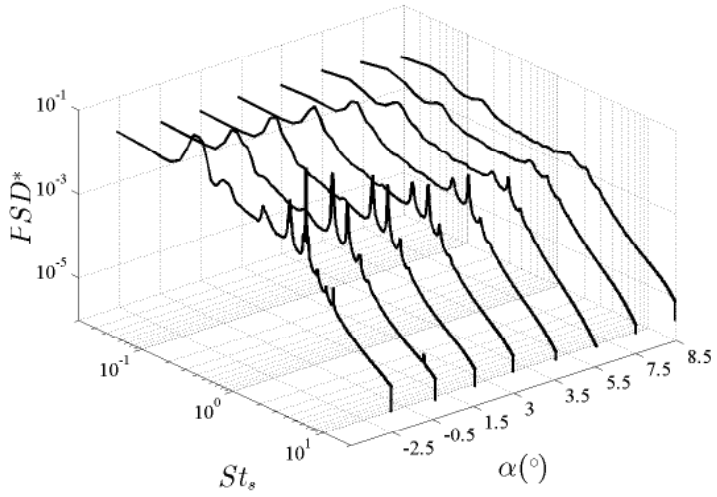

Figure 7. Spectra near reattachment point (Location 3 from Figure 6) for $Re_c = 1.71 \times 10^6$.

Table 2. Binwidth center of main spectral peaks with 16 Hz resolution.

α	$St_{s,1}$	$St_{s,2}$	$St_{s,3}$	$St_{s,4}$
3°	0.128	1.524	2.276	3.029
5.5°	0.137	1.482	2.223	3.022
8.5°	0.148	1.336	2.004	N/A

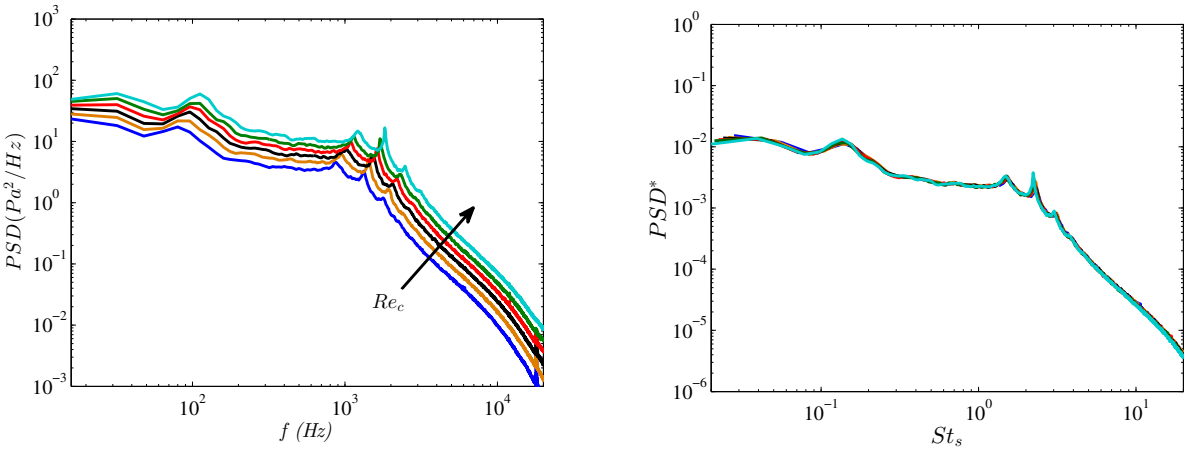

(a) (b)

Figure 8. Reynolds number effect near reattachment point (Location 3 from Figure 6) in (a) dimensional and (b) nondimensional units.

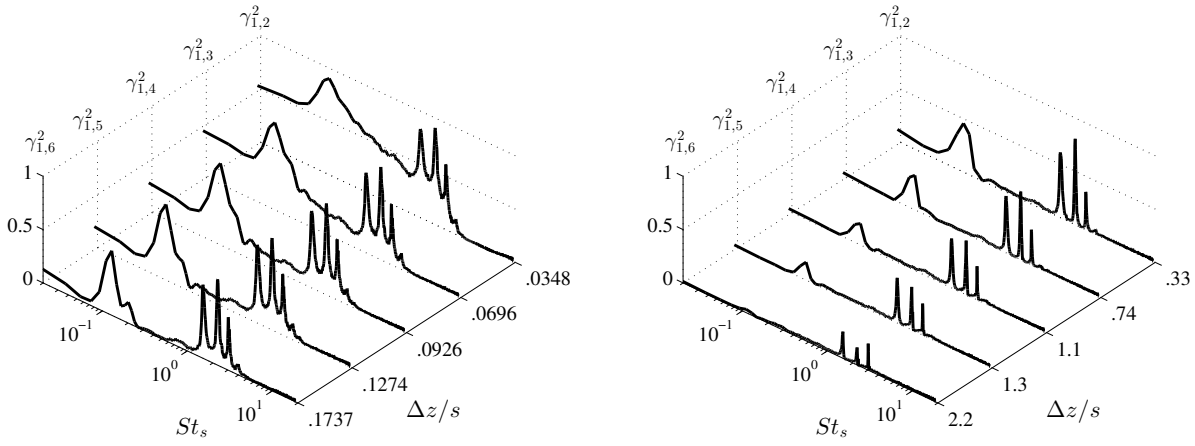

(a) (b)

Figure 9. Spanwise coherence, $\gamma^2_{1,n}$ where $n = 1 - 6$ at $\alpha = 3^\circ$ for the (a) small and (b) large span array.

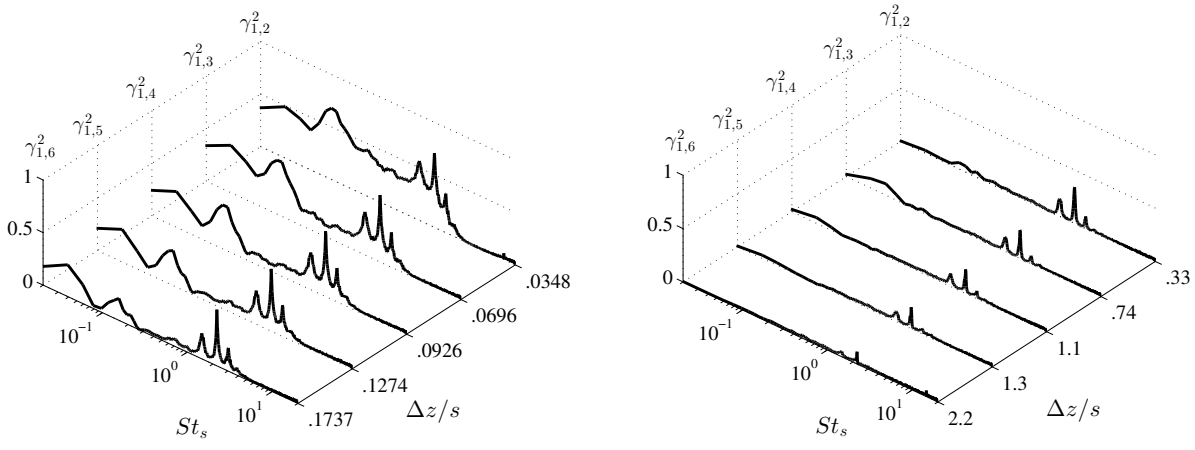

(a) (b)

Figure 10. Spanwise coherence, $\gamma^2_{1,n}$ where $n = 1 - 6$ at $\alpha = 5.5^\circ$ for the (a) small and (b) large span array.

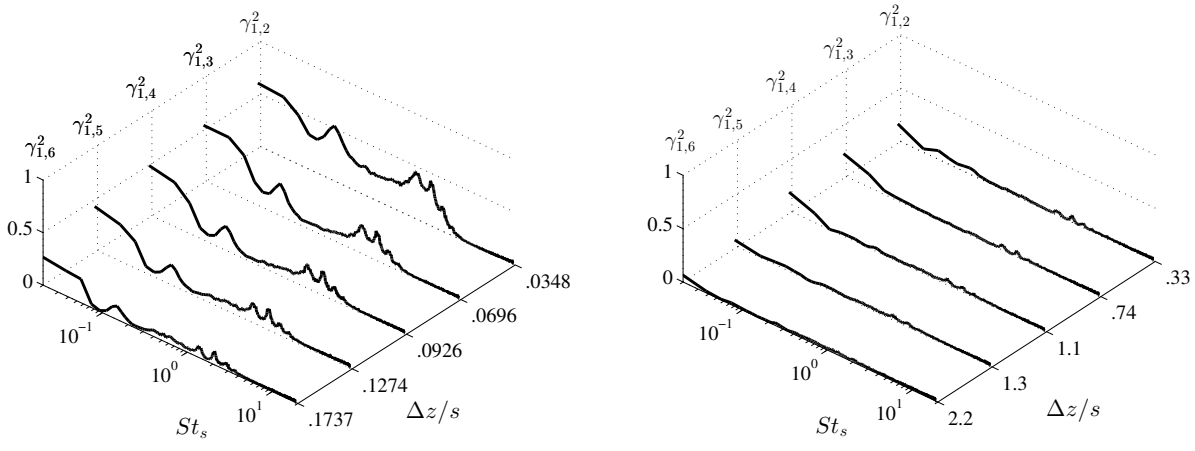

(a) (b)

Figure 11. Spanwise coherence, $\gamma^2_{1,n}$ where $n = 1 - 6$ at $\alpha = 8.5^\circ$ for the (a) small and (b) large span array.

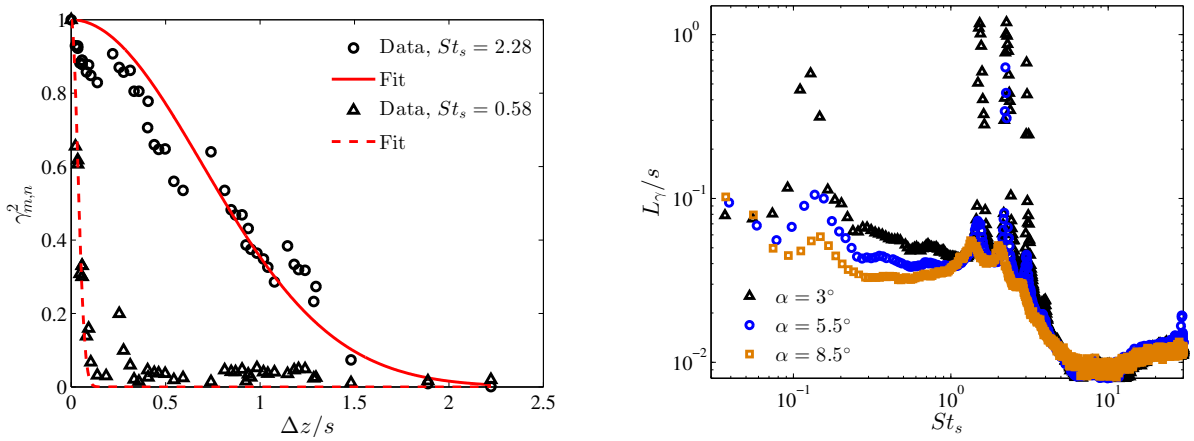

Figure 12. Spanwise coherence of pressure fluctuations near reattachment location: (a) Example of functional fit, and (b) coherence length as a function of Strouhal number.

III.C. SPIV Measurements

Stereoscopic PIV provides quantitative information of the velocity field in the recirculation region and the slat shear layer by providing a map of all three velocity components over a planar segment determined by the laser sheet and the field of view of the camera. Previous PIV measurements[12] of the 30P30N configuration with a slightly different slat contour offered valuable insights into the slat cove flow field while simultaneously providing a database for the validation of computational simulations. However, tunnel blockage was significantly higher in their case, which modified the aerodynamic loading relative to the free-air configuration and made it necessary to simulate the tunnel domain as opposed to using the free flight boundary conditions that are desirable for characterizing the noise radiation. On the other hand, the results in section III.A demonstrate that the present configuration matches the aerodynamic loading on the flight configuration, allowing a direct comparison with numerical simulations for the free-air case. The case $\alpha = 5.5°, Re_c = 1.71 \times 10^6$ was selected for the PIV measurements.

Figure 13 presents the average velocity magnitude and streamlines—both in good agreement with Lockard and Choudhari[13] when comparing the separation streamline and main element stagnation point. The exact reattachment location is difficult to ascertain due to the loss of near surface data. Spanwise vorticity in Figure 14 is also very similar, in both the average and instantaneous sense. Investigating the set of instantaneous snapshots, two cove states similar to those defined by Jenkins et al.[12] are identified. Upon reattachment on the slat underside, the vortical structures produced by the shear layer tend to either get trapped in the recirculation (State 1) or convect out through the slat and main element gap (State 2). This is additional evidence that the reattachment point is oscillating on the surface. Note that in the instantaneous figure, the small points of high vorticity outside of the shear layer are non-physical due to seeding issues. Also, our measurements tend to enlarge the initial shear layer due to the combination of its small thickness relative to vector resolution and the averaging process.

The distribution of mean and *rms* spanwise velocity component in the slat cove region is depicted in Figure 15. The mean component is less than 0.06 U_∞ and peaks in the shear layer and recirculation core, while the fluctuations from the mean can exceed 0.04 U_∞. The nonzero mean velocity in the spanwise direction may seem surprising, but at least two possible reasons may have contributed to this finding. Previous studies have documented the presence of local spanwise variations in time averaged properties of a plane shear layer.[25] The short-scale three-dimensionality in the mean flow could possibly account for a nonzero mean w across the planar PIV measurement. Another cause for the nonzero mean of w velocity component may be related to the large scale three-dimensionality in the mean flow, caused by the presence of end walls. To ascertain the relative importance of these two factors, similar measurements across multiple cuts along the spanwise direction are necessary.

The distribution of turbulent kinetic energy (TKE) has been plotted in Figure 16a. An important outcome of this work allows the spanwise component to be included in the TKE calculation. $\langle v'v' \rangle$, where $\langle \cdot \rangle$ denotes

the ensemble average, is found to be dominant while $\langle u'u' \rangle$ and $\langle w'w' \rangle$ are relatively smaller but comparable in magnitude to each other. Further decomposition of the Reynolds stresses illustrates which components are important contributors to the overall turbulence. Since TKE contains information about the normal components, the $\langle u'v' \rangle$ component is plotted in Figure 16b. Near the initiation of the shear layer, there is positive correlation between the fluctuations in u and v; however, these two fluctuations eventually become out of phase near the reattachment point. Since the shear layer is nearly horizontal at the cusp and nearly vertical at reattachment, this correlation has some local significance in these regions.

Section cuts in the shear layer are useful to understand its evolution. Seven cuts are made as depicted in Figure 13a and are identical to the BANC-III problem statement.[4] Various quantities are plotted in Figure 17 where the figure's abscissa follows each black line from left to right (passing through the shear layer in the PIV image plane). The velocity gradient is largest near the cusp and flattens out along its trajectory. L6 and L7 show the acceleration of fluid through the gap at the end of the path lengths. The profiles of spanwise vorticity and TKE are similar to each other, displaying prominent peaks in the center of the shear layer while flattening out away from the peak as a result of turbulent mixing.

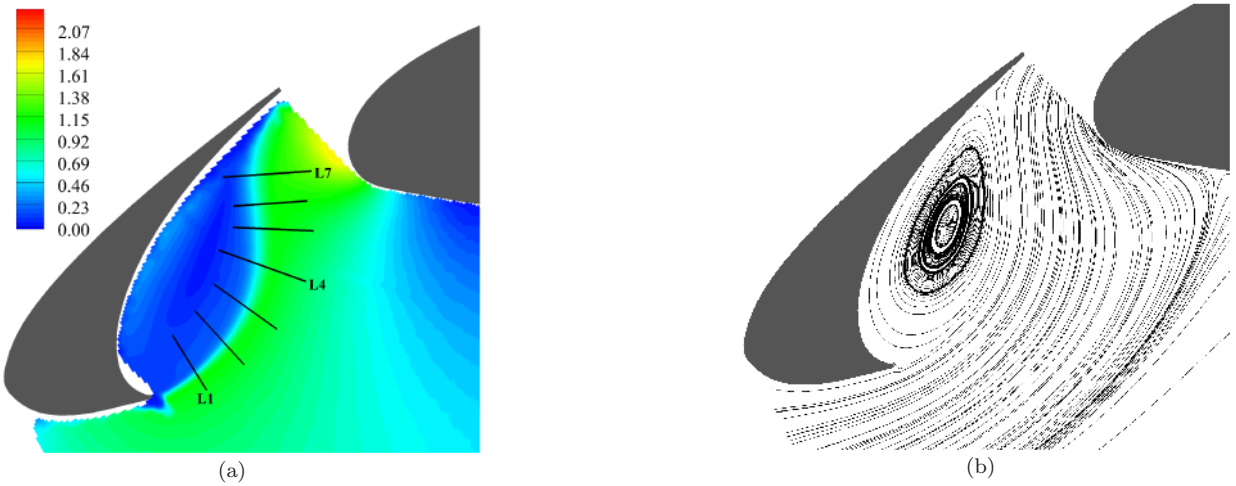

(a) (b)

Figure 13. Averaged SPIV results (a) Velocity magnitude, $|V|/U_\infty$, and (b) streamlines.

(a) (b)

Figure 14. Spanwise vorticity, $\omega_z c/U_\infty$, (a) averaged and (b) instantaneous.

IV. Conclusion and Future Work

Surface and off body flow measurements were conducted to characterize the slat region of the 30P30N three-element high-lift configuration. Nominal flow conditions ranged from $Re_c = 1.2 - 1.71 \times 10^6$ ($U_\infty = 41 - 58$ m/s) and measurements were obtained at multiple angle of attacks, with a focus on $\alpha = 3°, 5.5°, 8.5°$. Steady and unsteady surface pressure measurements were acquired for the selected flow conditions. Tunnel effects were quantified and the results demonstrated that a nearly spanwise homogeneous mean flow was

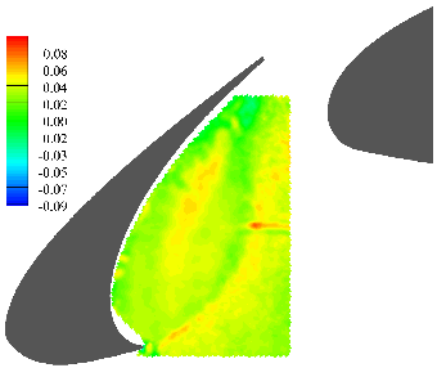

(a)

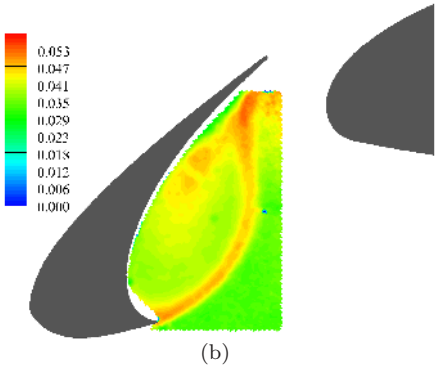

(b)

Figure 15. Spanwise velocity component (a) mean, $\langle w \rangle / U_\infty$ and (b) rms, $\langle w' \rangle / U_\infty$.

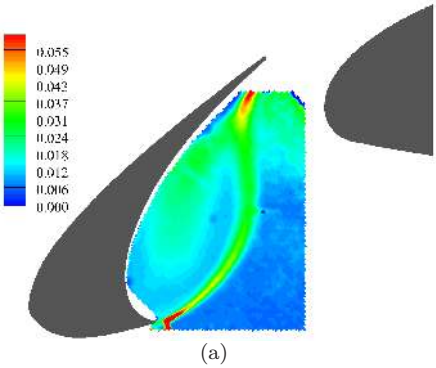

(a)

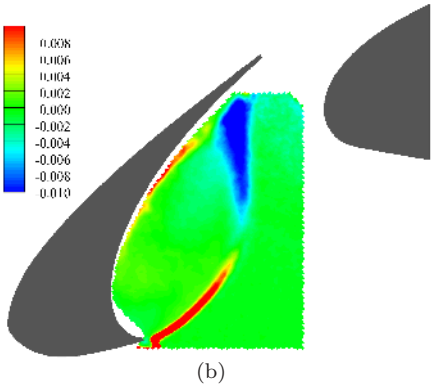

(b)

Figure 16. Turbulence quantities, (a)$TKE, 1/2(\langle u'u' \rangle + \langle v'v' \rangle + \langle w'w' \rangle)/U_\infty^2$ and (b) Reynolds stress component $\langle u'v' \rangle / U_\infty^2$.

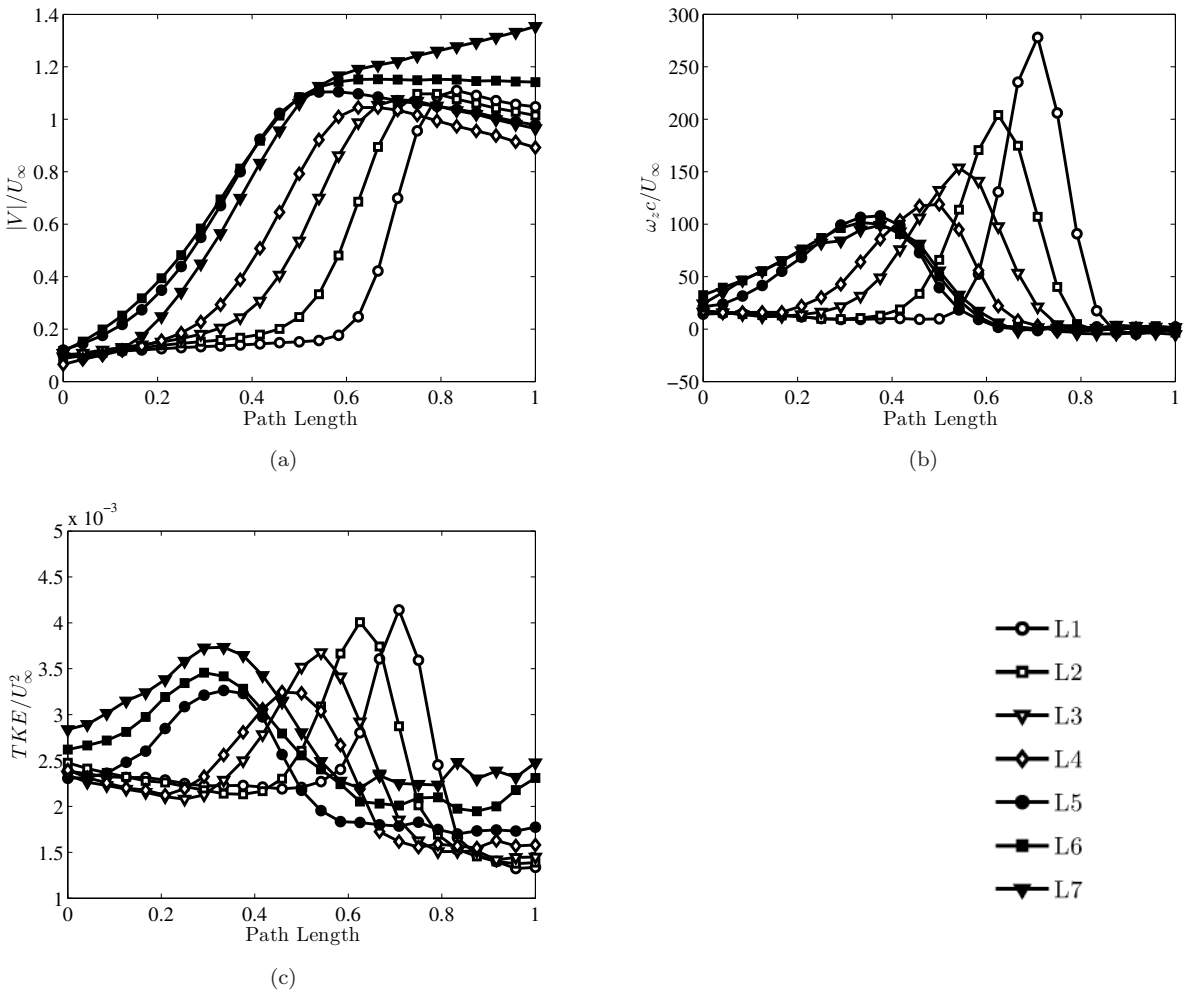

Figure 17. Velocity magnitude (a), spanwise vorticity (b), and turbulent kinetic energy (c) for shear layer section cuts defined in Figure 13a. Data points are obtained using PIV grid resolution.

achieved across approximately one third of the model span near the center plane. At all three angles of attack, the steady pressures within the core spanwise region compared well with previous numerical simulations for the free-air configuration[21] and no correction to the measured data was found necessary to account for the tunnel wall effects.

The amplitude of pressure fluctuations on the slat surface was found to scale well with the freestream dynamic pressure, so that there was no significant dependence on the Reynolds number across the range of measurements. The frequency spectra of slat pressure fluctuations showed up to four prominent peaks. Slight Strouhal differences in these peaks ($St_{s,1}$ increases with α, $St_{s,2-4}$ decrease) were evident, suggesting there are more appropriate scaling parameters. The amplitudes of these peaks decrease when the angle of attack is increased. The three highest frequency peaks are found to be in a harmonic relationship and likely due to a resonance induced by the shear layer. Spanwise coherence of these fluctuations was found to decay in a shorter distance at the larger angles of attack. A Gaussian fit provided a reasonable (albeit imperfect) approximation to the spanwise coherence distribution at a fixed frequency so that a coherence length could be used as a single metric for the coherence of slat pressure fluctuations. PIV measurements showed reasonable agreement with previous computations and also provided three-dimensional turbulence statistics. These measurements have expanded the experimental database for the benchmark 30P30N configuration, paving the way for more thorough validation of simulation-based techniques for airframe noise prediction.

Future work will build upon the presented results to gain further insight into the flow physics and specific mechanisms that are responsible for the generation of the farfield noise. PIV measurements will be extended by phase-locking to the narrow-band frequency peaks found in the unsteady surface pressure. A major goal for the follow-on effort will be to provide further insights into the nature of the flow phenomena that are responsible for each of the spectral features discussed herein. Additionally, simultaneous sampling of the unsteady surface pressure and PIV will be conducted to enable spatio-temporally resolved estimates of the velocity field via stochastic estimation techniques. This, in turn, would allow measurement-based predictions of the surface pressure field, which can be projected using Curle's analogy to predict the farfield noise.

V. Acknowledgments

The work reported here is performed as part of a subcontract to The Boeing Company under the NASA Contracts NNL10AA05B and NNL13AE76P. The authors would like to thank the task monitor, Dr. Yueping Guo of The Boeing Company, for his support and guidance. Also a thanks to Douglas Weber and Christopher Cagle at NASA Langley for their help with model design, the NASA Langley Machine shop for fabricating the instrumented slat model, and Dan Neuhart and Luther Jenkins for their generous advice with model assembly. Thanks are also due to the FSU machinists Bobby Avant and Adam Piotrowski for tunnel modifications.

References

[1]Golub, R., Rawls, J., and Russell, J., "Evaluation of the Advanced Subsonic Technology Program Noise Reduction Benefits," NASA TM 2005–212144, May 2005.

[2]Guo, Y., "Slat noise modeling and prediction," *Journal of Sound and Vibration*, Vol. 331, No. 15, 2012, pp. 3567–3586.

[3]Klausmeyer, S., Papadakis, M., and Lin, J., "A Flow Physics Study of Vortex Generators on a Multi-Element Airfoil," AIAA Paper 96–0548, 1996.

[4]Choudhari, M., Khorrami, M., and Lockard, D., "Slat Cove Noise: 30P30N 3-Element, Simplified High-Lift Configuration (Modified Slat)," Guidelines for Category 7 of BANC-II Workshop, 2012.

[5]Roger, M. and Perennes, S., "Low-Frequency Noise Sources in Two-Dimensional High-Lift Devices," AIAA Paper 2000–1972, 2000.

[6]Pott-Pollenske, M., Alvarez-Gonzalez, J., and Dobrzynski, W., "Effect of Slat Gap/Overlap on Farfield Radiated Noise," AIAA Paper 2003–3228, 2003.

[7]Terracol, M., Manoha, E., and Lemoine, E., "Investigation of the Unsteady Flow and Noise Sources Generation in a Slat Cove: Hybrid Zonal RANS/LES Simulation and Dedicated Experiment," AIAA Paper 2011–3203, 2011.

[8]Choudhari, M. and Khorrami, M., "Effect of Three-Dimensional Shear-Layer Structures on Slat Cove Unsteadiness," *AIAA Journal*, Vol. 45, No. 9, 2007, pp. 2174–2186.

[9]Khorrami, M., Singer, B., and Berkman, M., "Time-Accurate Simulations and Acoustic Analysis of Slat Free Shear Layer Introduction," *AIAA Journal*, Vol. 40, No. 7, 2002, pp. 1284–1291.

[10]Tam, C. and Pastouchenko, N., "Gap Tones," *AIAA Journal*, Vol. 39, No. 8, 2001, pp. 1442–1448.

[11]Khorrami, M., Choudhari, M., and Jenkins, L., "Characterization of Unsteady Flow Structures Near Leading-Edge Slat: Part II: 2D Computations," AIAA Paper 2004–2802, 2004.

[12]Jenkins, L., Khorrami, M., and Choudhari, M., "Characterization of Unsteady Flow Structures Near Leading-Edge Slat: Part I: PIV Measurements," AIAA Paper 2004–2801, 2004.

[13]Lockard, D. and Choudhari, M., "Noise Radiation from a Leading-Edge Slat," AIAA Paper 2009–3101, 2009.

[14]Dobrzynski, W., "Almost 40 Years of Airframe Noise Research: What Did We Achieve?" *Journal of Aircraft*, Vol. 47, No. 2, 2010, pp. 353–367.

[15]Choudhari, M., Lockard, D., Macaraeg, M., Singer, B., Streett, C., Neubert, G., Stoker, R., Underbrink, J., Berkman, M., Khorrami, M., and Sadowski, S., "Aeroacoustic Experiments in the Langley Low-Turbulence Pressure Tunnel," NASA TM 2002–211432, 2002.

[16]Kolb, A., Faulhaber, R., Drobietz, R., and Grunewald, M., "Aeroacoustic Wind Tunnel Study on a Two-Dimensional High-Lift Configuration," AIAA Paper 2007–2447, 2007.

[17]Khorrami, M. and Choudhari, M., "Application of Passive Porous Treatment to Slat Trailing Edge Noise," NASA TM 2003–212416, May 2003.

[18]Smith, M., Chow, L., and Molin, N., "Attenuation of Slat Trailing Edge Noise Using Slat Gap Acoustic Liners," AIAA Paper 2006–2666, 2006.

[19]Klausmeyer, S. and Lin, J., "Comparative Results from a CFD Challenge Over a 2D Three-Element High-Lift Airfoil," NASA TM 1997–112858, May 1997.

[20]Griffin, J., Schultz, T., Holman, T., Ukeiley, L., and Cattafesta, L., "Application of multivariate outlier detection to fluid velocity measurements," *Experiments in Fluids*, Vol. 49, No. 1, 2010, pp. 305–317.

[21]Choudhari, M., Lockard, D., Khorrami, M., and Minec, R., "Slat Noise Simulations: Status and Challenges," Inter-Noise 2011, May 2011.

[22]Rumsey, C., Lee-Rausch, E., and Watson, R., "Three-dimensional effects in multi-element high lift computations," *Computers & Fluids*, Vol. 32, No. 5, 2003, pp. 631–657.

[23]Rossiter, J., "Wind-Tunnel Experiments on the Flow over Rectangular Cavities at Subsonic and Transonic Speeds," Aeronautical Research Council Reports and Memoranda 3438, 1966.

[24]Chen, J. and Fang, Y., "Strouhal numbers of inclined flat plates," *Journal of Wind Engineering and Industrial Aerodynamics*, Vol. 61, No. 2, 1996.

[25]Bell, J., Plesniak, M., and Mehta, R., "Spanwise Averaging of Plane Mixing Layer Properties," *AIAA Journal*, Vol. 30, No. 3, 1992, pp. 835–837.